Measurement of mixed-mode fracture characteristics of an epoxy-based adhesive using a hybrid digital image correlation (DIC) and finite elements (FE) approach

A. Taylor Owens [a,*], Hareesh V. Tippur [b]

[a] *US Army CCDC Aviation & Missile Center, Redstone Arsenal, AL 35898, USA*
[b] *Department of Mechanical Engineering, Auburn University, AL 36830, USA*

ARTICLE INFO

ABSTRACT

The present work seeks to investigate the semi-circular beam (SCB) geometry for studying mixed-mode (mode-I and -II) fracture of a rubber-toughened epoxy-based adhesive material. A hybrid experimental-numerical technique involving digital image correlation technique and finite element modeling is formulated for extracting the *J*-integral values and stress intensity factors (SIF). Experiments are conducted to compare the results extracted using the hybrid approach with those from regression analysis of measured crack tip displacements. Critical stress intensity factors are extracted for a range of mode mixities. Based on a curve fit of the test data, the mode I and mode II critical stress intensity factors are estimated to be 1.19 MPa/$\sqrt{m}$ and 1.46 MPa/$\sqrt{m}$, respectively. The specimen geometry, loading configuration and experimental setup are critically assessed to identify and understand effects and outcomes associated with friction at the supports and unintended support asymmetry on stress intensity factors. Several different techniques are also discussed for mapping measured displacement data onto the finite element model for reliably extracting the fracture parameters. Recommendations are made regarding best practices for using this geometry and the associated hybrid technique for extracting fracture parameters.

1. Introduction

1.1. Background

The study of material fracture is fundamental to understanding damage tolerance and reliability of structures. Cracks and crack-like defects in a structure cause local amplification of stresses. The complexity of this locally amplified state of stress often cannot be accurately captured using conventional techniques such as finite element analysis where coarse meshes produce averaging effects that significantly under-predict local maximum stresses and thus, tend to be non-conservative. Conversely, extremely fine meshes can be computationally burdensome and riddled with numerical artifacts. Fracture-based analyses, on the other hand, can be used to understand stresses near such defects and the conditions under which those defects would catastrophically extend. This leads to a better design of the effect of a flaw size on structural performance reduction during single and repeated loading events.

The field of fracture mechanics is continually evolving as new engineered materials are introduced regularly that warrant investigation and often necessitate appropriate techniques to do so. In this context, lightweight composite materials, though prone to manufacturing or ser-

vice induced cracks/defects, have been incorporated into a wide range of applications in recent years. For instance, in commercial aviation, rising operating costs have driven aircraft manufacturers to pursue structural weight reduction by adopting advanced composite materials. In the automotive and sporting goods industries, composite materials have been widely used to reduce weight, improve performance, and even reduce cost relative to traditional materials. Fiber reinforced composite materials have even found widespread application in commercial infrastructure applications such as utility poles and fiber optic cable sheathing as well.

While composite materials offer a multitude of advantages from the standpoint of specific strength and specific stiffness, fracture considerations are an important factor in critical structural applications. Of specific relevance to the current research is fracture behavior of adhesives which play an important role in composite structures. A challenge that persists with many composite structural applications is the ability to fasten secondary components and structures to the primary composite structures. Due to their inherent low bearing strength, traditional methods of fastening using bolts, screws, or rivets is often challenging. Additional material thickness is often required near fasteners to enable effective transfer of loads. These local material buildups can be signifi-

cant and contribute to not only increases in weight but also additional cost and processing complexity. These make attachments through adhesive bonding methods attractive. The disadvantage, however, is the difficulty to assess the structural performance of adhesively bonded joints. This is attributed to three key contributors: the elastic mismatch between the adhesive and adherend, the complex stress distribution in the adhesive layer, and potential manufacturing-induced defects in the adhesive and/or adherend. The current work seeks to investigate fracture behavior in an epoxy adhesive with dual objectives: (a) to develop an improved understanding of fracture geometries that lend themselves to the study a wide range of mode-mixities in isotropic fracture problems, and (b) to develop a methodology based on ubiquitous engineering tools that can be conveniently implemented by practitioners studying a broad range of fracture problems.

This paper is organized into five sections. First a brief overview of the use of digital image correlation in the field of fracture mechanics is given. Second, a hybrid approach that utilizes full-field experimental digital image correlation displacement data and a finite element model is outlined for extracting fracture parameters. Third, an experimental investigation is carried out to assess the overall approach. Fourth, the critical stress intensity factors are measured and fracture envelope is developed for an epoxy-based material for a range of mode mixities. Finally, several observations with respect to the experimental fracture specimen geometry, test fixture, and interpretation of test results are made.

1.2. Two-dimensional digital image correlation

Two-dimensional digital image correlation (DIC) is a technique for measuring full-field planar displacements/deformations of an object experiencing load. The method was introduced in the early 1980's [1–4] and has attained a great deal of popularity in recent years. The general principle involves applying a random pattern to the surface of an object of interest. As mechanical loads are imposed on the object, the random pattern/speckles follow the deformation of the surface of the object being tested. A digital camera is used to capture a series of speckle images as the object undergoes deformation during a loading event. Once the images are recorded, displacement fields can be computed by comparing subsequent images in the series with the reference image.

To describe the technique briefly, consider a set of two random speckle images, the first being an image the reference state, and the second in the deformed state. Each image is segmented into an array of sub-images (or, subsets, facets), as illustrated in Fig. 1.

The image correlation process seeks to track the position of each sub-image in the reference state as it follows surface deformations. This is accomplished by matching gray scale features of the subsets of the reference image with those in the deformed state.

A technique that is commonly used for tracking sub-image features is based on the normalized cross-correlation coefficient, C_{CC}, evaluated as:

$$C_{CC} = \frac{\sum_{(i,j)\in S} \left(f\left(\tilde{x}_{ref,i}, \tilde{y}_{ref,j}\right) - f_m \right)\left(g\left(\tilde{x}_{cur,i}, \tilde{y}_{cur,j}\right) - g_m \right)}{\sqrt{\sum_{(i,j)\in S} \left[f\left(\tilde{x}_{ref,i}, \tilde{y}_{ref,j}\right) - f_m \right]^2 \sum_{(i,j)\in S} \left[g\left(\tilde{x}_{cur,i}, \tilde{y}_{cur,j}\right) - g_m \right]^2}} \tag{1}$$

where f and g represent the intensity distributions within the subsets of the reference and deformed images respectively and are defined as:

$$f_m = \frac{\sum_{(i,j)\in S} f\left(\tilde{x}_{ref,i}, \tilde{y}_{ref,j}\right)}{n(S)} \tag{2}$$

$$g_m = \frac{\sum_{(i,j)\in S} g\left(\tilde{x}_{cur,i}, \tilde{y}_{cur,j}\right)}{n(S)} \tag{3}$$

where n is the number of points within the subset S and:

$$\tilde{x}_{cur,i} = x_{ref,i} + u_{rc} + \frac{\partial u}{\partial x_{rc}}\left(x_{ref,i} - x_{ref,c}\right) + \frac{\partial u}{\partial y_{rc}}\left(y_{ref,j} - y_{ref,c}\right) \tag{4}$$

$$\tilde{y}_{cur,j} = y_{ref,j} + v_{rc} + \frac{\partial v}{\partial x_{rc}}\left(x_{ref,i} - x_{ref,c}\right) + \frac{\partial v}{\partial y_{rc}}\left(y_{ref,j} - y_{ref,c}\right) \tag{5}$$

$$\tilde{x}_{ref,i} = x_{ref,i} + u_{rr} + \frac{\partial u}{\partial x_{rr}}\left(x_{ref,i} - x_{ref,c}\right) + \frac{\partial u}{\partial y_{rr}}\left(y_{ref,j} - y_{ref,c}\right) \tag{6}$$

$$\tilde{y}_{ref,j} = y_{ref,j} + v_{rr} + \frac{\partial v}{\partial x_{rr}}\left(x_{ref,i} - x_{ref,c}\right) + \frac{\partial v}{\partial y_{rr}}\left(y_{ref,j} - y_{ref,c}\right) \tag{7}$$

The variables u and v represent displacements in the global x- and y-directions respectively. Quantities associated with the reference image are denoted by ref, and i and j subscripts are pixel locations relative to the center of the corresponding subset. Subscripts rr denote transformations within the reference image and rc denote transformations between reference and current images. The typical correlation process seeks to maximize the cross-correlation coefficient. By doing so, a given subset from the reference image can be tracked in the deformed image, and thus, the displacement of that subset will be known. This process is repeated for all subsets and all deformed images to create a full-field measure of displacements and the associated history.

1.3. DIC to study fracture

A number of researchers have utilized full-field measurement approaches to understand material fracture. Over-deterministic least-squares error minimization technique based on full-field optical measurements and analytical stress field solutions for evaluating opening-mode stress intensity factors in a cracked specimens, introduced by Sanford [5,6], has been a popular approach. Subsequently, others have reported utilizing measured displacements from digital image correlation [7–9] in conjunction with least-squares regression analysis to identify fracture parameters. Kirugulige [10,11] extended one of these approaches to the investigation of mixed-mode behavior under dynamic loading conditions. Yoneyama [12] demonstrated the extraction of the *J*-integral from cracked specimen using displacement data from digital image correlation. Yates, et. al. [13] investigated the effects of fatigue on cracked specimens using the least-squares approach with displacements from digital image correlation method. Their research included extraction of the so-called *T*-stress values as well.

2. Hybrid DIC-FE approach

The current work seeks to utilize full-field displacement data from digital image correlation measurements coupled with a finite element model to reliably extract fracture parameters for an edge-cracked specimen. This approach is beneficial as it couples an easy-to-implement displacement measurement technique adaptable to a wide range of problems with a data extraction methodology that is based on proven algorithms in mature software tools. The basic work flow is as follows: full-field displacements are measured in two orthogonal in-plane directions using DIC, the coordinates of the DIC output points are utilized to build a finite element mesh, and then, robust algorithms within a commercial finite element package are used to extract domain integral quantities and decompose them into mixed mode stress intensity factors. The general concept is similar to the coupled experimental-numerical approach used by Tippur and Chiang [14] where displacements measurements from Moiré experiments were mapped onto a finite element model to extract fracture parameters. Dubois, et. al. [15] has recently utilized a coupled approach that includes digital image correlation and finite element analyses to extract fracture parameters from experiments on timber materials. The measured displacement data was used to compute the kinematic state of the crack faces, while the finite element solution was used to evaluate the stress intensity factors. Isaac, et al. [16] utilized a similar hybrid approach to investigate effects of build orientation on fracture in additively manufactured materials.
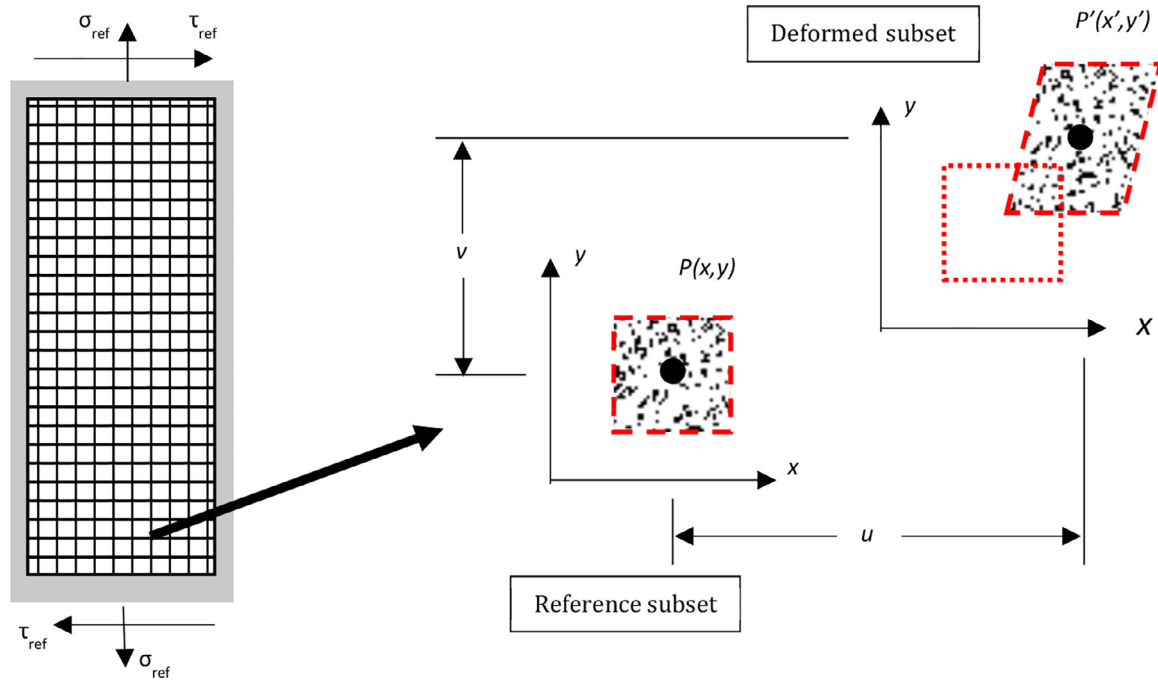
Fig. 1. Digital image correlation sub-image illustration.

2.1. Digital image correlation details

In the present work, the Ncorr [17] software was utilized for performing DIC. Ncorr is an open source code developed in the Matlab software environment for performing subset-based two-dimensional DIC. It utilizes well-documented and accepted solution practices and provides flexibility for developers. The normalized cross-correlation (as defined in Eq. (1)) is used for providing the initial guess for subset matching at the seed points. Sub-pixel accuracy is then achieved by computing using the Inverse Compositional Gauss-Newton (ICGN) method to perform a nonlinear optimization using the normalized least squares criterion, C_{LS}:

$$C_{LS} = \sum_{(i,j)\in S} \left[\frac{f\left(\tilde{x}_{ref,i}, \tilde{y}_{ref,j}\right) - f_m}{\sqrt{\sum_{(i,j)\in S}\left[f\left(\tilde{x}_{ref,i}, \tilde{y}_{ref,j}\right) - f_m\right]^2}} - \frac{g\left(\tilde{x}_{cur,i}, \tilde{y}_{cur,j}\right) - g_m}{\sqrt{\sum_{(i,j)\in S}\left[g\left(\tilde{x}_{cur,i}, \tilde{y}_{cur,j}\right) - g_m\right]^2}} \right]^2 \tag{8}$$

this prevents the normalized cross-correlation computation from having to be made for all subset points. The process serially works its way out from the initial seed point. Even though this process cannot be directly parallelized, Ncorr, breaks the region of interest up into smaller regions. This reliability-guided digital image correlation (RG-DIC) computation procedure can then be executed across a number of computer processors in parallel.

2.2. Speckle patterning

The ability to maximize the cross-correlation coefficient noted above is dependent on the uniqueness of each of the sub-images. Thus, the technique is founded on the general characteristics of the pattern/speckles on the object surface. The pattern must be random and generally isotropic. High contrast between the speckles and the background as well as consistency in the size of the speckles is also desirable with the black speckles covering approximately 50% of the white background. The desirable speckle size is related to the resolution of the camera, and the typical speckle size spanning 3-5 pixels of the sensor is recommended. Patterns consisting of large variations in the size and spacing of speckles can result in correlation difficulties. Since the speckle size
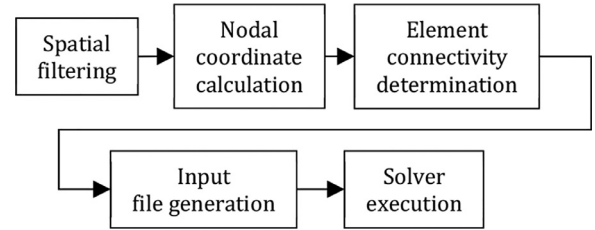

Fig. 2. Digital image correlation data post processing.

and imaging optics are directly related to the measurement resolution, patterning techniques have been developed to address image correlation problems across a myriad of length scales from nanoscale all the way to problems involving deformations in massive geographic features on the earth's surface. Thus, the patterning technique is only limited by the user's imagination and creativity.

2.3. Extraction of fracture parameters

Many commercial finite element (FE) packages offer options for the extraction of fracture parameters. Specifically, the Abaqus finite element software package offers a multitude of options for extraction of fracture parameters using path independent contour integration based approaches. For the present effort, a script was developed to manage this process. The Ncorr code first creates a Matlab data file with the u- and v-displacement data from the DIC analysis. The data is stored in two arrays where each entry contains a displacement value associated with the spatial location of a given subset centroid. Once the displacements are known, the workflow as shown in Fig. 2 is followed.

2.4. Treatment of noise

One important consideration of utilizing the DIC technique is the treatment of noise in the measured displacements. Due to the discontinuous nature of the displacement data due to the crack, generic smoothing techniques (e.g., moving average filters, etc.) are not appropriate in

this particular application. Also, noise is common to many experimental techniques, and it becomes more important with DIC in situations where displacement measurement is not the end objective. The objective of the current work is to extract contour integral quantities out of the measured displacement data. Thus, derived quantities such as strain and/or stress are of importance. It is, therefore, necessary to properly treat noise such that in the stress and displacement gradient-based contour integral quantities can be accurately extracted. To that end, an image processing technique was adapted to post-process the displacement data prior to mapping it into the finite element model. A guided filter was chosen to improve the smoothness of the DIC data but minimize the smoothing effect in regions where the large gradients are attributed to the stress field and not experimental noise. The basic concept of guided filtering involves choosing a square window of data surrounding a data point of interest (i.e., $N \times N$ data points) and taking into account the local statistics of the window to calculate the output values of the filtered data at the point of interest. The output at a given data point q can be calculated based on a weighted average of the data points p from the sub-array of data points.

$$q_i = \sum_j W_{ij}(I)p_j \tag{9}$$

where i and j are spatial coordinates within the window, and the filtering kernel, W, is a function of the guidance image or guidance data set. The guidance data set can be formed beforehand based on knowledge of features within the image such as edges. As proposed by He, et al., [18], the output q at a given data point is a linear transform of the guidance data set, I, calculated from the coefficients, a_k and b_k, in a window or sub-array of data points, w_k, as:

$$q_i = a_k I + b_k \tag{10}$$

where the coefficients, a_k and b_k, are defined as:

$$a_k = \frac{\frac{1}{\omega} \sum_{i \in w_k} I_i p_i - \mu_k \bar{p}_k}{\sigma_k^2 + \epsilon} \tag{11}$$

$$b_k = \bar{p}_k - a_k \mu_k \tag{12}$$

The filtering input data is given as p, with $\bar{p}_k$ being the average of the data within the sub-array of data. The mean intensity value within the sub-array of the guidance data set is μ, σ_k^2 is the variance, ω is the number of data points in the sub-array of the guidance data set, and ϵ is a regularization parameter that penalizes the contributions of large values of a_k. Thus, the value of ϵ results in an increased or decreased degree of smoothing. The filtered output at each data point is calculated multiple times because each data point is involved in multiple overlapping sub-arrays of data. Thus the final output of a given data point can be computed as the average of all the individual computations of the output for that data point.

This filtering technique has a few interesting characteristics that are especially applicable to the current work. First and foremost is that this smoothing technique has an intrinsic edge-preserving property. Considering an area where the gradients are steep, the variance can be very high. An example of this would be at an edge of the specimen or, more importantly, adjacent to one of the crack faces. A window of data points that is centered over an edge would contain very high local variance. Because the edges of the specimen can be identified in the image, the image and the subsequent output displacement data can be used as a guide for the filter and thus mitigate this effect from the local variance. Filtering techniques such as moving average filters result in significant unwanted smoothing near edges. Using the guided approach, the edge is largely preserved. Alternate edge preserving filters can cause gradient reversal issues. The technique proposed in [18] alleviates this issue. In general, more smoothing occurs in areas with low variance and less smoothing occurs in areas with high variance while generally preserving edges and gradients.

2.5. Assembly of finite element mesh

Once the smoothing calculation has been performed, the script calculates the coordinates of each of the subset points based on the known pixel size, subset size, and subset spacing. The grid of DIC output points is structured with uniform spacing in the x- and y-directions. Once the nodal coordinates are known, the script utilizes the array indices of the nodal position data to establish the element connectivity using the Abaqus element connectivity convention where the first node is in the lower right quadrant. Other nodes of the element are ordered in a counter-clockwise direction. Once the nodal positions and element connectivity have been determined, the script then writes the node and element data into a text file in the proper Abaqus input file order and syntax. Lastly, the script writes the material property definitions for the model, and the appropriate output requests to extract the fracture parameters of interest. The Abaqus structural solver is then be executed to compute the fracture parameter outputs.

2.6. Extraction of stress intensity factors

In order to extract the stress intensity factors for a given specimen, a contour integral technique can be utilized. The energy release rate can be computed using a domain (area) integral. The J-integral, as presented in Shih, et al. [19], is defined as:

$$J = \int_A \left(-W \delta_{ij} + \sigma_{ij} \frac{\partial u_j}{\partial x_1} \right) \frac{\partial q_1}{\partial x_1} dA, \ (i, \ j = 1, 2) \tag{13}$$

where A is the area of the domain or the area that includes the crack tip being evaluated, q_1 is a weighting function that equals 1 on the outer boundary of the domain and 0 on the inner boundary of the domain. This domain integral can be decomposed into the two stress intensity factors K_I and K_{II} for modes I and II, respectively, using the relationship:

$$J = \frac{1}{E} \left(K_I^2 + K_{II}^2 \right) \tag{14}$$

The Abaqus finite element software employs an interaction integral technique to partition J and extract the two stress intensity factors based on the technique described in [20].

3. Experimental verification

In order to explore the implementation of the proposed workflow, an edge-cracked semi-circular beam (SCB) geometry was selected. This geometry offers many attractive features in that it has the ability to produce a wide range of pure and mixed mode fractures.

3.1. Test specimen geometry

The SCB test specimen geometry was first introduced to study mechanics problems involving cored concrete and rock [21–23] cylinders. In the investigation of geological materials such as rocks, many tools exist for extracting specimens in the form of circular cylinders out of the ground. Those cylinders can readily be sliced into disks and then cut in half to produce the semi-circular geometry. The same is true for engineered materials such as concrete and asphalt. Test samples for many different physical measurements are based on cylindrical geometry due to the widespread use of the coring process. For these reasons, this specimen geometry is finding widespread use which warrants critical evaluation from the fracture mechanics community.

The general specimen geometry and loading configuration are illustrated in Fig. 3 where R is the radius of the specimen, a is the crack length, β is the crack angle with respect to the horizontal axis of the specimen, and S is the half span. The Cartesian crack tip coordinates are denoted by the x- and y-axes parallel and perpendicular to the crack, respectively. The corresponding crack tip polar coordinates r and θ are as shown.
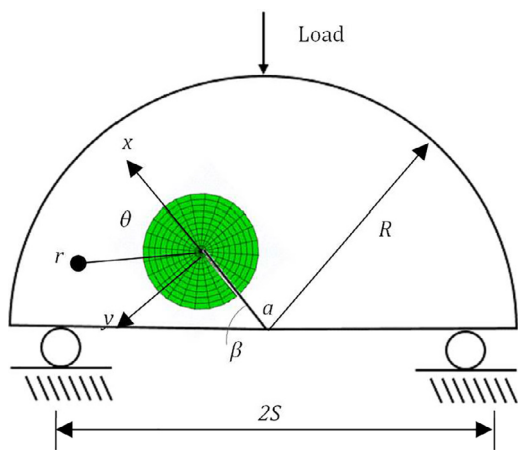
Fig. 3. Semi-circular beam bending test configuration shown with typical crack tip mesh.

As investigated in [23], the stress intensity factors at the crack tip, and therefore the mode mixity, are controlled by the geometric parameters of the test setup namely, R, a, β, and S. Normalized stress intensity factors, Y_I and Y_{II}, relative to the Griffith crack problem are defined as:

$$Y_{I;II} = \frac{K_{I;II}}{\sigma_0 \sqrt{\pi a}} \tag{15}$$

where K_I and K_{II} are the mode I and mode II stress intensity factors, $\sigma_0 = \frac{P}{2Rt}$, t being the specimen thickness.

3.2. Finite element model

Lim [23] explored the geometric effects and developed analytical expressions for mode I stress intensity factors for the SCB geometry. In order to characterize the relevant conditions for the present work and determine the desirable specimen dimensions, a similar process was followed. A finite element model was developed in Abaqus to mimic the geometry illustrated in Fig. 3 and explore the effects of different geometric parameters, namely the support span, crack inclination angle, and crack length. A base geometry of approximately 100 mm in diameter was chosen as a convenient and practical size from an experimental standpoint. For investigation of cast and/or injected polymeric materials, this was considered a reasonable specimen size for fabrication purposes. The model was meshed using 4-noded plane stress elements (Abaqus element type, CP4SR). The model contained approximately 17,000 elements and 17,000 nodes. On the lower edge of the test specimen, steel rollers were modeled. A steel platen was modeled at the top edge of the specimen with a load applied to the top of the platen. Frictionless contacts were assumed at the interface between the specimen and the adjacent components. A seam was created in the model to represent the initial edge crack. The mesh contained concentric rings of elements radiating out from the crack tip as illustrated in Fig. 3. At the physical crack tip in the model, the 4-noded elements were collapsed down to triangular elements by having two of the nodes reside at the same location.

3.3. Parametric study

The role of various span to radius (S/R) and crack length to radius (a/R) ratios on crack tip SIF were evaluated. Because overly long cracks can interact with the boundaries of the specimen, consideration was given to crack length. Also, the crack angle was considered because low crack angles can be difficult to fabricate and can result in fragile specimens. The effect of span and crack angle on mode I and mode II SIF's for three different a/R ratios is shown in Fig. 4.
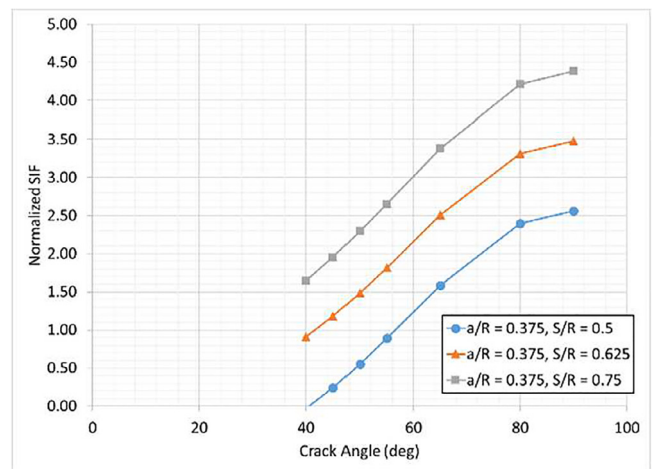
(a)
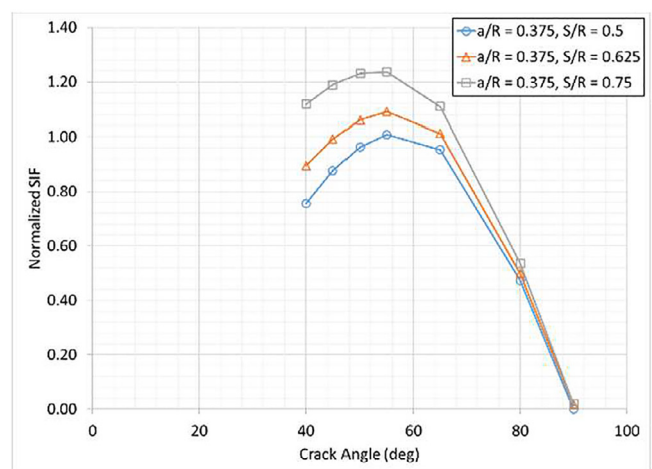
(b)

Fig. 4. Effect of varying span ratios and crack angles on (a) Mode I SIF and (b) Mode II SIF.

Based on the results of this study, seven different mode mixity conditions were selected for further experimental investigation, where the mode mixity is defined as $\varphi = \tan^{-1}(\frac{K_{II}}{K_I})$. The stress intensity factors and mode mixity are plotted in Fig. 5. These chosen inclination angles are denoted by the points on the graph. The corresponding mode mixities are shown with the gray line/symbols.

Evidently, the pure mode I and II cases occur at crack inclination angles of 90° and approximately 40°, respectively.

3.4. Test specimen fabrication

Rubber-toughened epoxy test specimens were fabricated for development and demonstration of this experimental procedure. An aluminum mold was fabricated with semi-circular cavities of the desired in-plane dimensions (100 mm diameter). Due to a large selection of epoxy-based adhesives that are commercially available, an epoxy formulation representative of a broad range of epoxy-based adhesive materials from the standpoint of elastic and failure properties was chosen. The epoxy formulation of interest is a basic mix of difunctional bisphenol A/epichlorohydrin derived liquid epoxy resin (EPON™ 828) with triethylenetetramine (EPIKURE™ 3234) curing agent. Based on manufacturer recommendations, the two components were mixed at a ratio of 100:13 by weight. Prior to mixing, the EPON™ 828 was heated to 66°C. Core-shell rubber particles were then mixed in at a ratio of 10% by weight. The mixture was then returned to 66°C for 2 hours to decrease
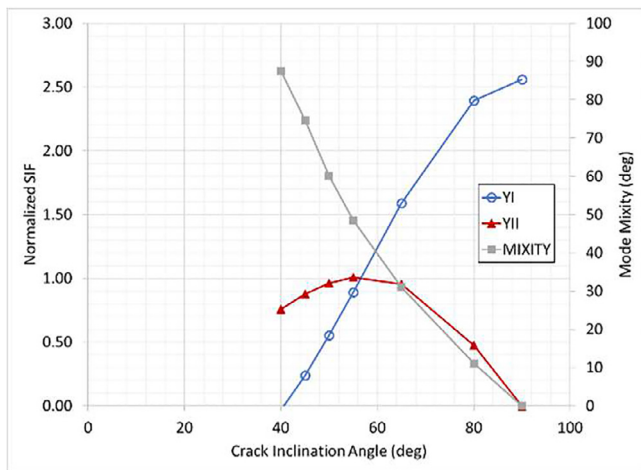
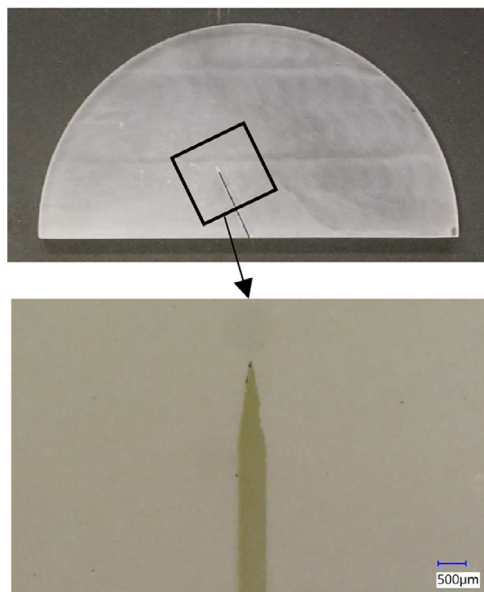**Fig. 5.** Normalized SIF and mode mixity for a/R = 0.375 and S/R = 0.5.

Fig. 6. Cast sample with an inclined crack (left) and close-up of the crack tip produced by razor blade (right).

Fig. 7. Compressive stress-strain response of the adhesive studied.

Table 1
Test specimen material properties.

Elastic modulus	3.00 GPa ($\pm$0.2 MPa)
Poisson's ratio	0.4
Density	1107 kg/m^3

and a nominal length of 25.4 mm were cast and cured. The true stress vs true strain data for the material is shown in Fig. 7. The elastic modulus for the linear model was calculated as the average slope across the range of 5,000 to 20,000 microstrain.

This compression testing was performed to provide an estimate of the elastic modulus of the material solely for the purposes of the development of this experimental approach. However, additional uniaxial testing is recommended to fully characterize the elastic response of the material and capture differences between tensile and compressive response, specimen geometric effects on axial response, and assumptions with respect to nonlinear material effects. While changes in these assumptions could alter some of the measured fracture properties, they would not be expected to alter the implementation of the method presented.

The assumed material properties of this epoxy formulation are summarized in Table 1.

3.5. Sample speckle patterning and assessment

Poor speckle patterns can result in unwanted measurement noise, while proper patterning techniques can achieve high quality results in DIC. For the present work, each of the test samples were painted with high quality flat white oil-based enamel paint. The surface was then sanded with fine grit sand paper to create a clean, smooth surface. Finally, a textured rubber stamp was utilized to transfer archival quality ink onto the test sample surface. The textured stamp had a nominal feature size of 180 microns. The stamp was applied to the specimen surface 5-6 times to achieve an acceptable quantity of speckles on the white background. With each application, the stamp was slightly rotated relative to the specimen to ensure a generally isotropic and stochastic pattern.

The speckle patterning technique for displacement measurement using DIC is often unique to a specific application. It is thus advantageous to assess the overall quality of the speckle pattern prior to proceeding with fracture characterization step. Several techniques have been proposed for speckle pattern quality determination. For the present work, the mean intensity gradient metric [25] was adopted. This metric has been demonstrated [25] as a reasonable global parameter for overall pattern assessment as mean bias error and standard deviation of mea-

the viscosity of the epoxy and allow entrapped air to escape the mixture. The mixture was then cooled to room temperature prior to adding the amine-based hardener. The epoxy mixture was then poured into the mold cavity. A sharp razor was inserted into the mold with the help of a template to align the razor blade in the desired orientation. A clip was attached to the razor blade to hold it in place while the epoxy cured. The samples were cured for approximately 24 hours at room temperature followed by a post cure for 2 hours at 93°C. The face of each test sample was then milled flat to the desired thickness of 6.4 mm.

This fabrication method was selected for two primary reasons. First, the cast-in-place razor blade forms a very repeatable crack with consistent lengths and consistent crack tip geometry from sample to sample. Second, it minimizes the amount of post-cure machining and thus any local damage in the vicinity of the crack tip. The only machining operation required after curing is to machine the top face of the sample down until the desired thickness is achieved. Photos of the finish machined test sample and the crack are shown in Fig. 6.

In order to estimate the elastic properties of the baseline material, compression testing was conducted with ASTM D 638 [24] as a guideline. Three compression specimens with a nominal diameter of 12.7 mm
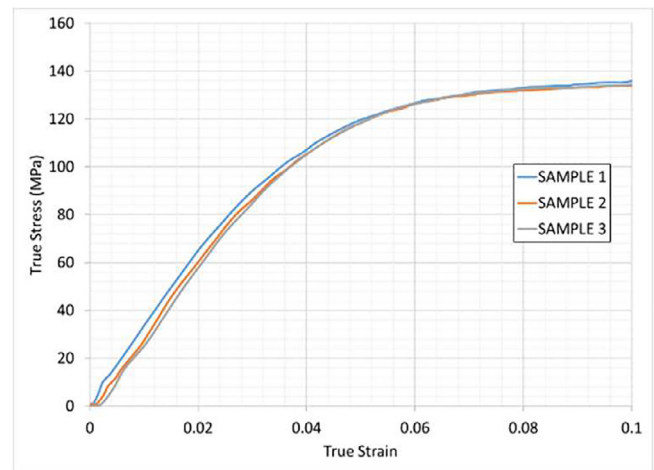
sured displacements are both strongly related to this metric. The mean intensity gradient is defined as:

$$\delta_f = \sum_{i=1}^{W} \sum_{j=1}^{H} \frac{|\nabla f(i,j)|}{(W \times H)} \tag{16}$$

where W and H are image width and height, $|\nabla f(i,j)| = \sqrt{f_x(i,j)^2 + f_y(i,j)^2}$ is the modulus of local intensity gradient and f_x and f_y are the local derivatives at a given pixel. The derivatives are computed using the central difference method. In [25], a mean intensity gradient in excess of 20 resulted in the lowest amounts of mean bias error and displacement standard deviation of all the speckle patterns analyzed. Sub-image samples were extracted from 5 images of 5 different test specimens. The average mean intensity gradient from those specimens was calculated to be 22.3.

3.6. Optical configuration

A Canon EOS T5i single lens reflex digital camera was used for acquiring 14 bit images with a sensor resolution of 5196 × 3464. The camera was placed such that the focal plane of the camera was approximately 1.1 meters from the face of the sample. With the approximate specimen width of 100 mm, the edges of the specimen are located at a maximum of approximately 2.5° from the optical axis. A 105 mm lens was utilized for imaging the specimen. With this lens, the pixel size was approximately 0.051 mm for each test.

3.7. Investigation of DIC and filtering parameters

A parametric study was conducted to investigate the appropriate subset size and subset spacing for this experimental work. The Ncorr software utilizes circular subsets. Subset radii ranging from 5 to 60 pixels, and subset spacing values ranging from 5 to 20 pixels were explored. A subset radius of 45 pixels and subset spacing of 5 pixels was selected for subsequent experiments.

As previously discussed, it is often advantageous to address noise when using digital image correlation. A numerical study was performed to qualitatively evaluate the effects of each of the filtering variables on the displacement results, specifically, the neighborhood size and filtering parameter. As the size of the neighborhood increases and higher values of the filtering parameter are chosen, it is possible to over smooth the image. There are also diminishing returns in terms of the effectiveness of the filter since points closer to the edge of the neighborhood for a given point have less effect on the filtered results. The performance of the filter is best illustrated using displacement contour plots at lower loads where more experimental noise is present. Fig. 8 shows a comparison of contour plots of an unfiltered data set compared to filtered counterparts from three different neighborhood sizes (3, 5, and 7). As can be seen, there is a noticeable difference in the noise in the filtered vs unfiltered contour plots. However, as the neighborhood size increases, the observed difference becomes less apparent. For the present work, a neighborhood size of 5 and a filtering parameter of 0.01 was chosen.

3.8. Comparison with baseline fracture parameter extraction techniques

As previously stated, one of the objectives of the present work is to assess the validity of the proposed hybrid DIC-FE displacement mapping approach to the study of fracture behavior. It is recognized that several techniques are available for extracting fracture parameters, and more specifically, contour/domain integral quantities and stress intensity factors from full-field displacement data measured using digital image correlation. However, the proposed hybrid DIC-FE approach offers several advantages. First, it offers the ability to leverage previously developed robust algorithms for domain integration and mode decomposition that are available in commercial finite element solvers. Second, it is suitable for a broad range of problems that include dissimilar material interface

crack problems. Further, this type of approach extends well to fractures involving more complex material behaviors as it can be utilized with a range of nonlinear and anisotropic material models.

To demonstrate the validity of this technique, an experiment was carried out for the five different crack orientations ranging from pure mode I to pure mode II. The first set of test specimens were monotonically loaded to a pre-defined load and then unloaded without failing the specimens. The stress intensity factors extracted using the proposed approach were first compared to results from the corresponding finite element model. Secondly, the more common approach of over-deterministic least-squares analysis of displacement data near the crack tip vicinity was utilized to calculate the stress intensity factors.

The over-deterministic least-squares results are computed using the equations reported in [26] for the crack sliding (u_x) and crack opening displacements (u_y):

$$u_x = \sum_{n=1}^{N} \frac{(K_I)_n}{2\mu} \frac{r^{\frac{n}{2}}}{\sqrt{2\pi}} \left\{ \kappa \cos\frac{n}{2}\theta - \frac{n}{2} \cos\left(\frac{n}{2} - 2\right)\theta + \left\{ \frac{n}{2} - (-1)^n \right\} \cos\frac{n}{2}\theta \right\}$$
$$+ \sum_{n=1}^{N} \frac{(K_{II})_n}{2\mu} \frac{r^{\frac{n}{2}}}{\sqrt{2\pi}} \left\{ \kappa \sin\frac{n}{2}\theta - \frac{n}{2} \sin\left(\frac{n}{2} - 2\right)\theta + \left\{ \frac{n}{2} - (-1)^n \right\} \sin\frac{n}{2}\theta \right\} \tag{17}$$

$$u_y = \sum_{n=1}^{N} \frac{(K_I)_n}{2\mu} \frac{r^{\frac{n}{2}}}{\sqrt{2\pi}} \left\{ \kappa \sin\frac{n}{2}\theta + \frac{n}{2} \sin\left(\frac{n}{2} - 2\right)\theta - \left\{ \frac{n}{2} + (-1)^n \right\} \sin\frac{n}{2}\theta \right\}$$
$$+ \sum_{n=1}^{N} \frac{(K_{II})_n}{2\mu} \frac{r^{\frac{n}{2}}}{\sqrt{2\pi}} \left\{ -\kappa \cos\frac{n}{2}\theta - \frac{n}{2} \cos\left(\frac{n}{2} - 2\right)\theta + \left\{ \frac{n}{2} - (-1)^n \right\} \cos\frac{n}{2}\theta \right\} \tag{18}$$

In the above equations, μ is the material shear modulus, and r and θ are the polar coordinates with crack tip as the origin and $\kappa = \frac{3-v}{1+v}$ for plane stress. The coefficients K_I and K_{II}, when $n = 1$, are the mode I and mode II stress intensity factors. For digital image correlation experiments, the u_x and u_y fields are known for a set of points in the polar coordinates r and θ, as illustrated in Fig. 3.

By selecting a group of points in the vicinity of the crack, a set of equations can be formed to determine the $(K_I)_n$ and $(K_{II})_n$. Using an over-deterministic approach, the experimental crack opening displacement can be used for extracting mode I fracture components whereas the crack sliding displacements can be used for mode II fracture components. However, it has been shown that by transforming experimental in-plane Cartesian displacements into radial (u_r) and angular (u_q) displacements, more accurate SIFs can be found in mixed mode problems [9]. That is, the Cartesian displacement components can be transformed into polar components as shown in Eqs. (19)-(21).

$$\begin{Bmatrix} u_r \\ u_\theta \end{Bmatrix} = \begin{bmatrix} \cos\theta & \sin\theta \\ -\sin\theta & \cos\theta \end{bmatrix} \begin{Bmatrix} u_x \\ u_y \end{Bmatrix} \tag{19}$$

$$u_{rk} = \left\{ \sum_{n=1}^{N} (K_I)_n f_{In}(r_k, \theta_k) + \sum_{n=1}^{N} (K_{II})_n f_{IIn}(r_k, \theta_k) \right\} \cos\theta_k$$
$$+ \left\{ \sum_{n=1}^{N} (K_I)_n g_{In}(r_k, \theta_k) + \sum_{n=1}^{N} (K_{II})_n g_{IIn}(r_k, \theta_k) \right\} \sin\theta_k$$
$$+ T_x \cos\theta_k + T_y \sin\theta_k \tag{20}$$

$$u_{\theta k} = \left\{ \sum_{n=1}^{N} (K_I)_n f_{In}(r_k, \theta_k) - \sum_{n=1}^{N} (K_{II})_n f_{IIn}(r_k, \theta_k) \right\} \sin\theta_k$$
$$+ \left\{ \sum_{n=1}^{N} (K_I)_n g_{In}(r_k, \theta_k) + \sum_{n=1}^{N} (K_{II})_n g_{IIn}(r_k, \theta_k) \right\} \cos\theta_k$$
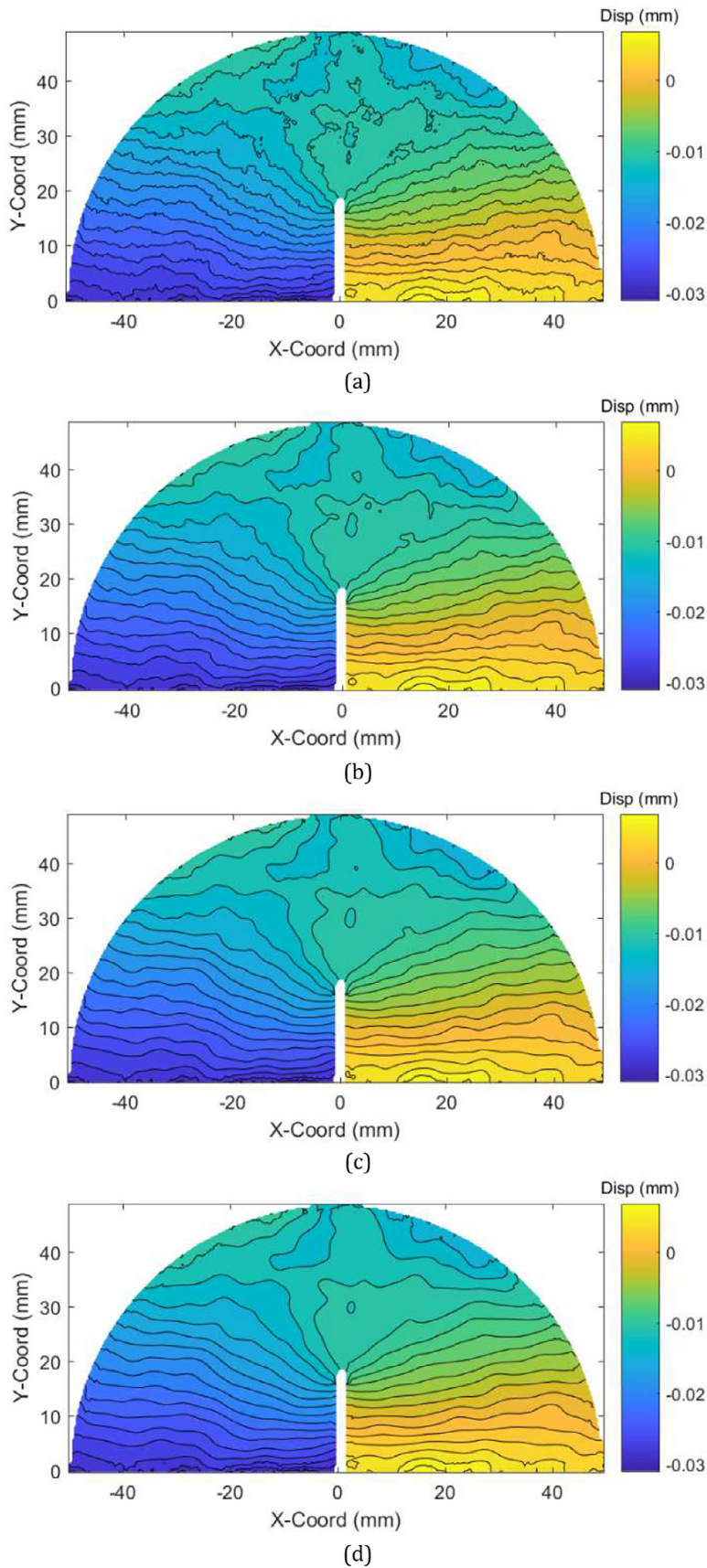$$- T_x \cos\theta_k + T_y \sin\theta_k \tag{21}$$

Fig. 8. Effect of filtering on displacement contour noise: (a) Unfiltered, (b) Neighborhood size, n = 3, (c) n = 5, (d) n = 7.
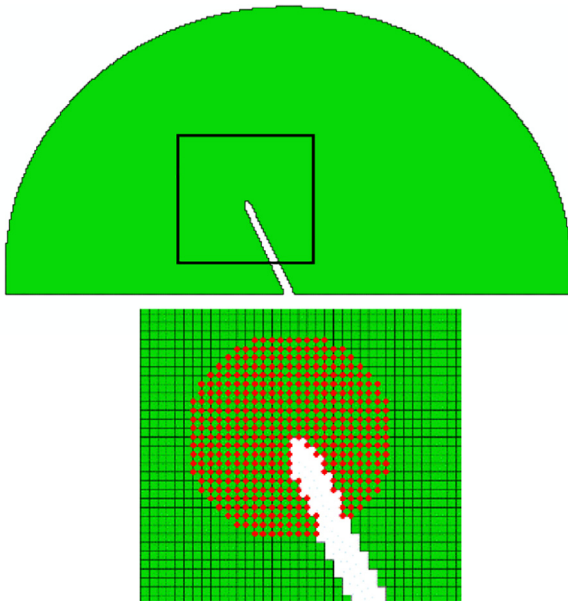
Fig. 9. Example of points considered in domain integral calculation.
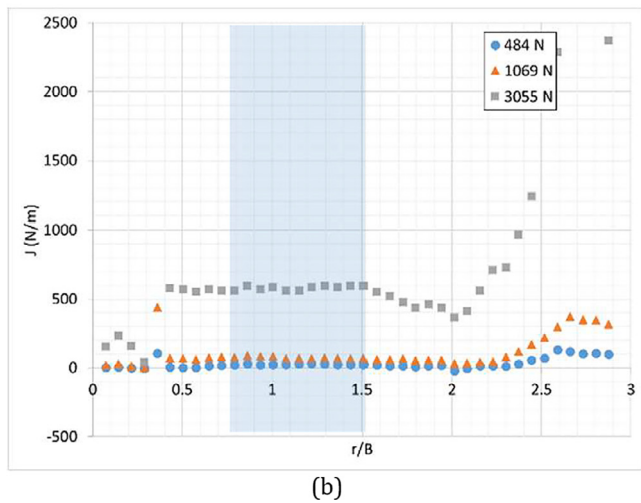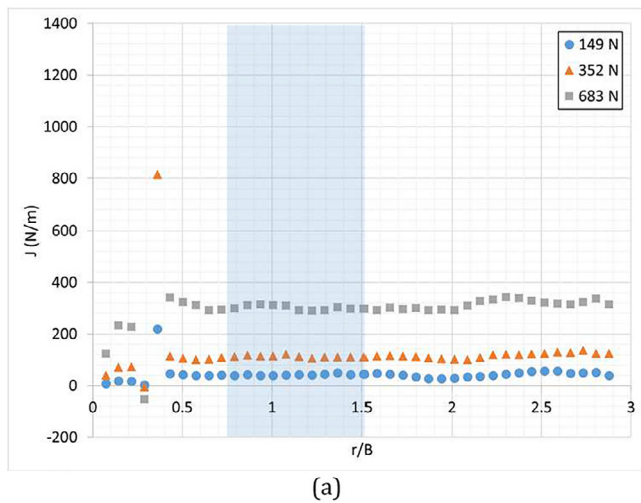

(a)

(b)

Fig. 10. Path independence of the J-integral from hybrid DIC-FE approach at different load steps for (a) pure Mode I test, (b) pure Mode II test.
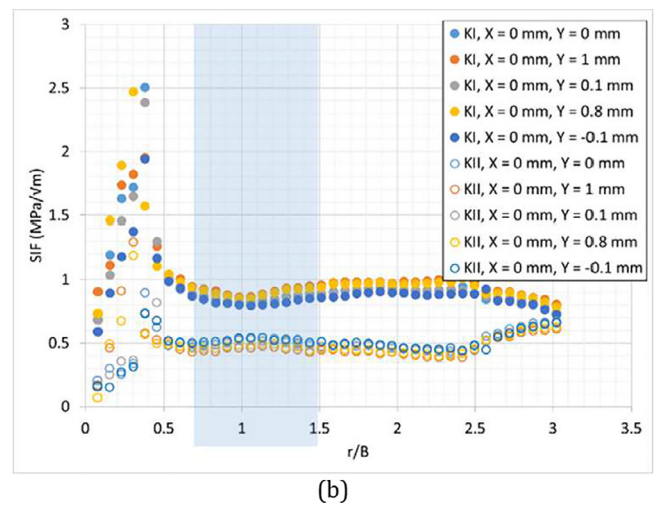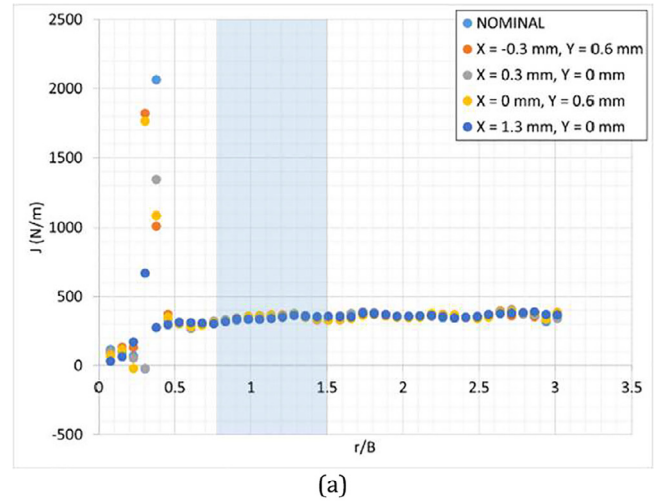

(a)

(b)

Fig. 11. Sensitivity of crack tip position selection for (a) the J-integral for mode I case (load = 840 N) and (b) KI and KII for a mixed mode case (crack angle = 65°, load = 1200 N).

where f and g are the functions from Eqs (17) and (18) and T_x and T_y are terms representing rigid body motion. Using this technique, these equations can be expanded out to any number of higher order terms. Experimental displacement data was extracted in the region $0.5 \leq {^r/_B} \leq 1.5$ and $-120° \leq \theta \leq 120°$. The over-determined equation set with $n = 3$ was formed and solved for minimizing the least-squares error to compute values of K_I, K_{II}, T_x, and T_y.

3.9. Comparison of results

Initial tests were conducted with a three-point bend fixture that utilized a roller at each of the support points and a flat platen to apply the load at the top of the specimen. It should be noted that the sensitivity of this specimen geometry to frictional effects at the supports and symmetry was first noticed and analyzed numerically. It was found to be an important consideration for practical implementation. Critical evaluation and further discussion of these results is detailed in the Appendix-A. The tests were conducted on a Tinius Olsen uniaxial load test frame. The specimens were loaded under displacement control at a rate of 0.25 mm/min. The camera was controlled remotely to acquire images at uniform intervals of 1 second. A 44.5 kN capacity load cell (accuracy = 0.04% of full scale) was used to measure the applied load. The Ncorr software was used to perform the speckle image correlations to quantify displacements. The measured displacement data and associ-
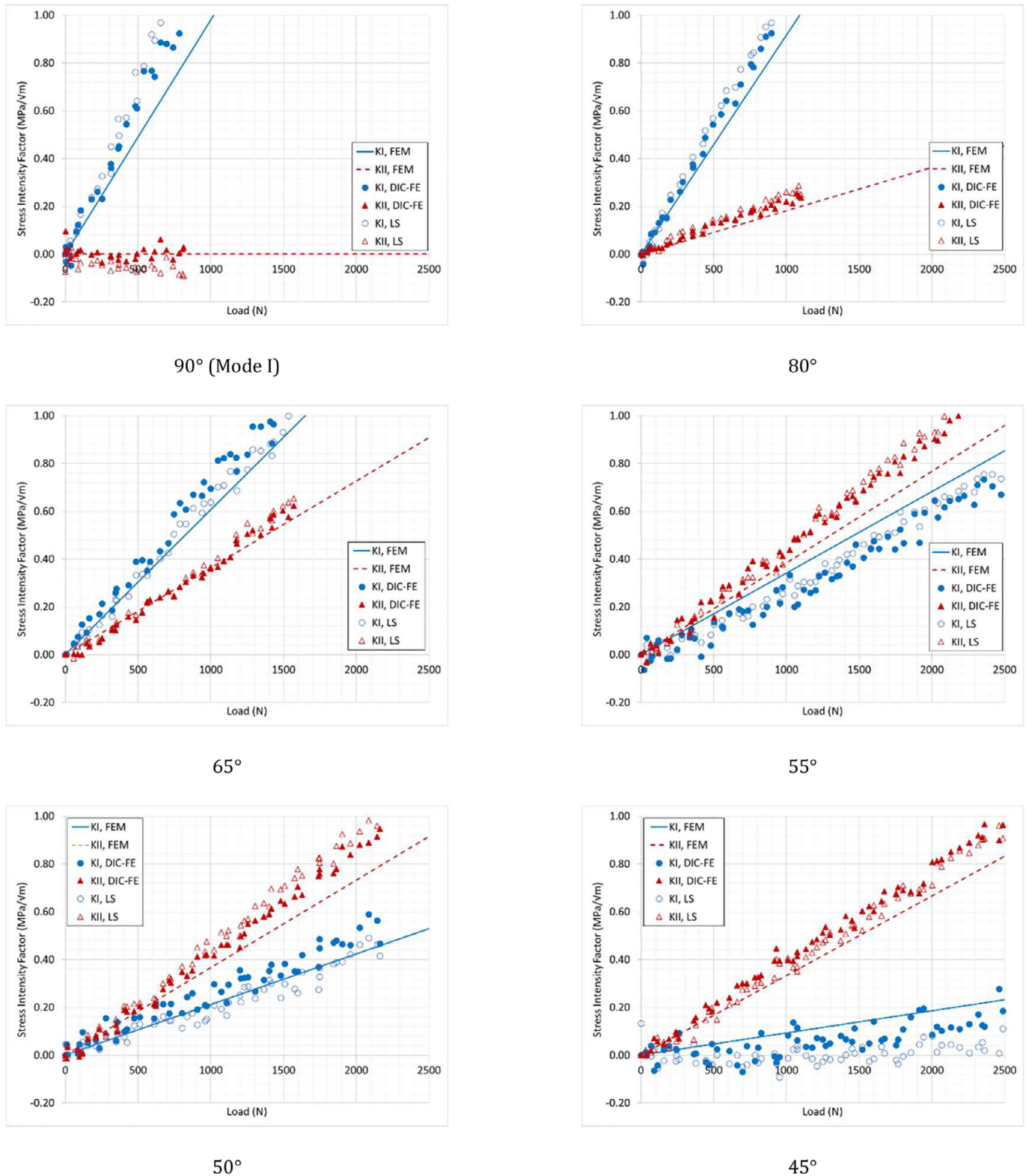
90° (Mode I)

80°

65°

55°

50°

45°

Fig. 12. Stress intensity factor extracted for different mode mixities.

ated DIC output coordinate locations were used to directly build a finite element mesh as previously described. Based on the subset spacing (5 pixels), and the pixel scale factor (~0.051 mm), the resulting distance between neighboring output points was 0.30 mm.

It is important to first verify that the contour integral quantified using the proposed methodology is indeed path independent. Abaqus by

default performs the contour integral computation for individual sets of elements that enclose the crack tip. To verify the path independence of the J-integral, successive contours must be extracted at increasing radial extents from the crack tip. The specifics of this computation can be configured by the user. Depending on how the output request is configured, the elements considered in each contour integral computation can
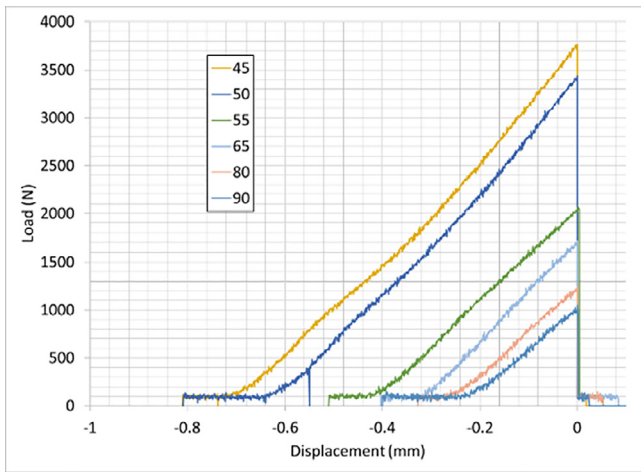
Fig. 13. Load histories for each crack inclination angle. Crosshead displacement of zero corresponds to crack initiation in each case.

Fig. 14. Comparison of mode-mixity for different crack angles in the SCB specimen with the corresponding FEM computations.
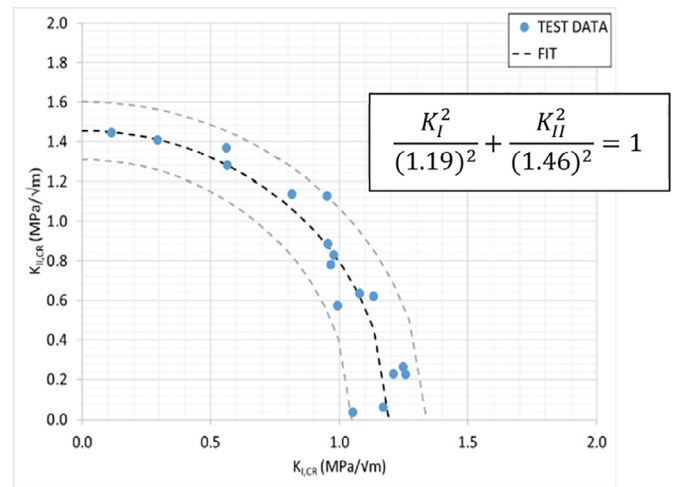

Fig. 15. Envelope of critical stress intensity factors. The data generally fall within one standard deviation of the band of elliptical curve fit.
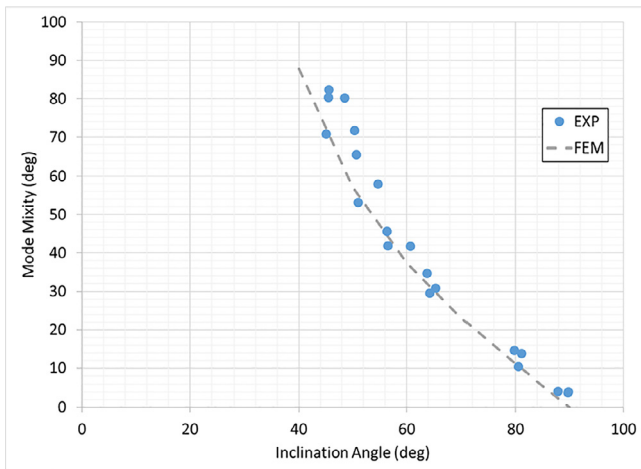
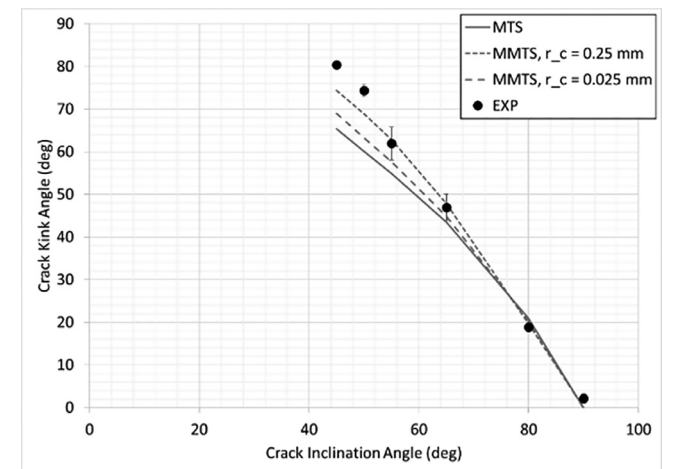$$\frac{K_I^2}{(1.19)^2} + \frac{K_{II}^2}{(1.46)^2} = 1$$

Fig. 16. Comparison of crack propagation direction with FE predictions.

be automatically determined by the Abaqus pre-processor, or it can be specified by the user. In the present work, circular contours of elements were manually specified as illustrated in Fig. 9. Further discussion on choice of this process is detailed in Appendix A.

The J-integral output is plotted as a function of the ratio of r/B in Fig. 10(a) for the pure mode I case and in Fig. 10(b) for the near mode II case, where r is the radial distance from the crack tip and B is the specimen thickness. A value of $r/B = 3$ corresponds to a contour radius of 19.1 mm.

Generally, as the radius of the contour increases, the J-integral values remain relatively constant. This does not hold true for points approximately within the zone $r/B = 0.5$ (or ~3 mm) from the crack tip. This can be attributed to a combination of factors including crack tip stress triaxiality, inelastic deformations, errors in identifying the crack tip position, and potential mesh size dependencies. Otherwise, the value remains relatively constant, even at very low loads for the mode I case. For the mode II case, the value remains relatively constant for $0.5 \leq r/B \leq 2$. Outside of this range, the individual contours reach the edge of the test specimen, and affects the J-integral values.

Another advantage of this technique is that the selection of crack tip position is much less critical when compared to the least-squares approach. To ascertain this, the mode I experimental data were analyzed by intentionally selecting erroneous locations for the crack tip. Those erroneous locations were chosen across a range of positions within ap-

proximately 1.5 mm of the nominal location of the crack tip (as identified in the speckle image). This was considered to be a large range relative to an experimentalist's ability in most cases at this specimen scale. The computed J-integral values for the mode-I case are plotted in Fig. 11(a) for a select load level. Evidently, they are invariant relative to the crack tip position selection. A similar exercise was performed for one of the mixed mode cases (65° crack inclination angle), and comparisons were made with respect to SIF computations. These comparisons, shown in Figs 11(b), indicate that the method is rather robust in this regard.

3.10. Mixed mode experiments

One sample from each crack orientation angle was loaded to a predefined load before failure to generate displacement data for extracting the fracture parameters namely K_I and K_{II} for comparing them with the ones from the baseline methods. The comparisons are plotted in Fig. 12 for the linear elastic finite element model (FEM), over-deterministic least-squares (LS) analysis, and the hybrid DIC-FE approach. The results generally agree well with each other for both mode I and mode II stress intensity factors. Note that the initial tests for the 90°, 80°, and 65° samples were performed to lower loads as they are expected to fail at lower loads due to the higher mode I contribution. Further discussion with respect to potential differences between the experiments and the linear finite element model are detailed in Appendix-B.
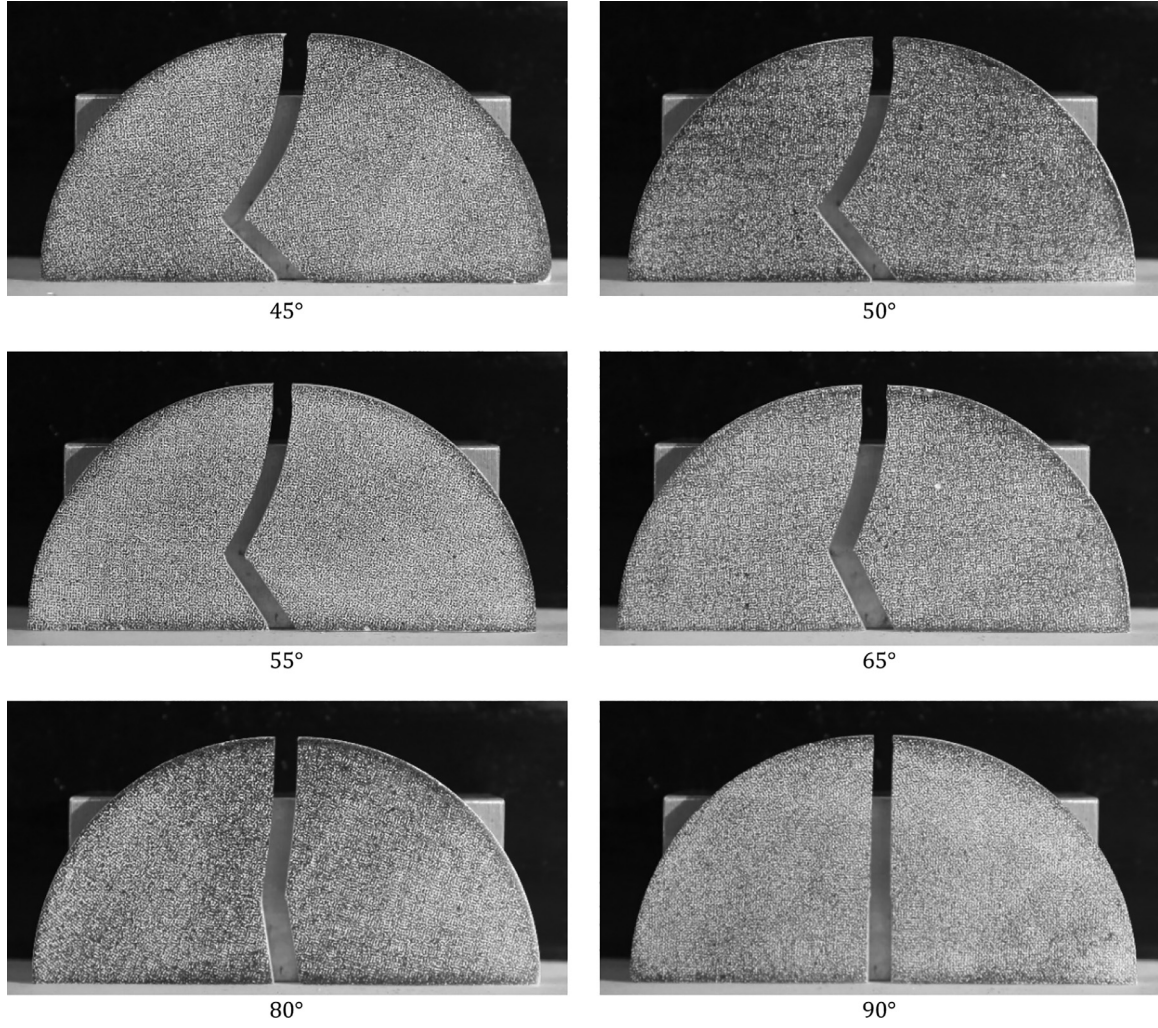
Fig. 17. Images of failed SCB test specimens.

4. Critical stress intensity factors

A series of fracture tests were performed to utilize this approach to extract the critical stress intensity factors across a range of mode mixities. Each of the test specimens exhibited brittle failure. The load histories, shown in Fig. 13, had a generally linear response up until failure at which time the load instantaneously released. The minor nonlinearities observed during the tests are attributed to fixture settling, nonlinear material response at the load point or supports, and/or rolling/sliding friction at the supports.

Multiple test samples were cast and tested for each crack inclination angle. The stress intensity factors for each mode were extracted at failure using the aforementioned technique. The mode mixity at failure was computed and plotted for different crack inclination angles.

The two critical stress intensity factors, K_{Icr} and K_{IIcr}, from each of the experiments are plotted as a crack initiation envelope in Fig. 15. The data points are shown only for results within one standard deviation of the elliptical curve fit.

For each crack inclination angle, the expected crack propagation angles were calculated using the conventional maximum tangential stress criterion using the load results and the finite element models. The tangential stress for a mixed mode crack as described in [27] is,

$$(\sigma_{\theta\theta})_{cr} = \frac{1}{\sqrt{2\pi r}} \cos\frac{\theta}{2}\left[K_{Icr}\cos^2\frac{\theta}{2} - \frac{3}{2}K_{IIcr}\sin\theta\right] + O\left(r^{\frac{1}{2}}\right) \quad (22)$$

where K_{Icr} and K_{IIcr} are the critical mode I and mode II stress intensity factors respectively. By taking the derivative with respect to the angular coordinate, θ, the angle of crack propagation can be found using:

$$\left[K_{Icr}\sin\theta_0 + K_{IIcr}(3\cos\theta_0 - 1)\right] = 0 \quad (23)$$

where θ_0 is the crack propagation direction. The higher order terms are considered to be negligible. For each test specimen, image analysis was used to measure the crack initiation direction. More recently, it has been suggested [28] that the so-called T-stress may play an important role in the crack initiation process. It is suggested that considering the T-stress in the maximum tangential stress computation provides better agreement with predicted crack propagation conditions. In this form, the modified maximum tangential stress criteria is computed (MMTS) using:

$$\sigma_{\theta\theta} = \frac{1}{\sqrt{2\pi r}} \cos\frac{\theta}{2}\left[K_I\cos^2\frac{\theta}{2} - \frac{3}{2}K_{II}\sin\theta\right] + T\sin^2\theta + O\left(r^{\frac{1}{2}}\right) \quad (24)$$

and thus the resulting derivative becomes:

$$\left[K_I\sin\theta_0 + K_{II}(3\cos\theta_0 - 1)\right] - \frac{16T}{3}\sqrt{2\pi r_c}\cos\theta_0\sin\frac{\theta_0}{2} = 0 \quad (25)$$

where T is the so-called T-stress, and r_c is a critical value of radial distance away from the crack tip and is considered to be a material parameter. The T-stress is related to the in-plane constraint effect and can affect the local crack growth mechanics. The T-stress is extracted from the linear finite element model using an auxiliary solution of a line load

applied in the plane of crack propagation and along the crack line as described in [29].

To assess these two sets of crack propagation direction, the values for a given crack inclination angle as measured from experiments were averaged for comparison with the finite element counterparts. The crack propagation directions, as calculated from Eq. (23) and (25), are compared to the experimental average crack propagation directions in Fig. 16. In general, the average propagation directions were fairly consistent with low standard deviations. The predicted values were generally lower than the observed ones, however, when the *T*-stress is considered, the agreement between the predicted propagation directions and the experimentally measured directions is much closer. The photographs of failed specimens are shown in Fig. 17.

The measurements from hybrid DIC-FE approach agree well with the predicted response from the finite element model as shown in Fig. 14.

5. Conclusions

Mixed mode fracture behavior of an epoxy-based adhesive is studied experimentally. A numerical study was undertaken initially to determine the relationships between crack inclination angle, support span, crack length, and mode mixity for a given specimen radius. Digital image correlation method was employed to measure in-plane deformations near cracks, and a data reduction technique was investigated for extracting fracture parameters by utilizing displacement measurements made using digital image correlation, and mapping the data into a finite element discretization. Several experiments were performed to evaluate the data reduction technique in Abaqus structural analysis environment, and it was shown to produce path-invariance with respect to the *J*-integral output. The interaction integral approach further allowed decomposition of the *J*-integral into individual mode I and mode II stress intensity factors. This approach was shown to be relatively insensitive to identification of crack tip position. Multiple experiments were performed to compare the measured stress intensity factors for several different mode mixities. Proper treatment of experimental noise in the measured displacement data and mapping of the displacement data onto the finite element model were also investigated in detail. The critical stress intensity factors were measured and reported across a range of mode mixities. The measured crack kink angles were also compared to predicted propagation angles using from conventional maximum tangential stress criteria as well as a modified tangential stress criteria that considers the effects of the so-called *T*-stress. Better agreement was found for the crack propagation angles when the effects of *T*-stress were included.

The results of this work demonstrate that the proposed hybrid technique is advantageous due to its convenience of implementation which enables use of a range of robust experimental and numerical fracture analysis tools. It can readily be extended for use in the study interfacial fracture investigations as well as nonlinear and anisotropic fracture problems.

Declaration of Competing Interest

The authors declare that they have no known competing financial interests or personal relationships that could have appeared to influence the work reported in this paper.

CRediT authorship contribution statement

A. Taylor Owens: Conceptualization, Methodology, Data curation, Formal analysis, Validation, Writing - original draft. **Hareesh V. Tippur:** Conceptualization, Methodology, Validation, Writing - review & editing.
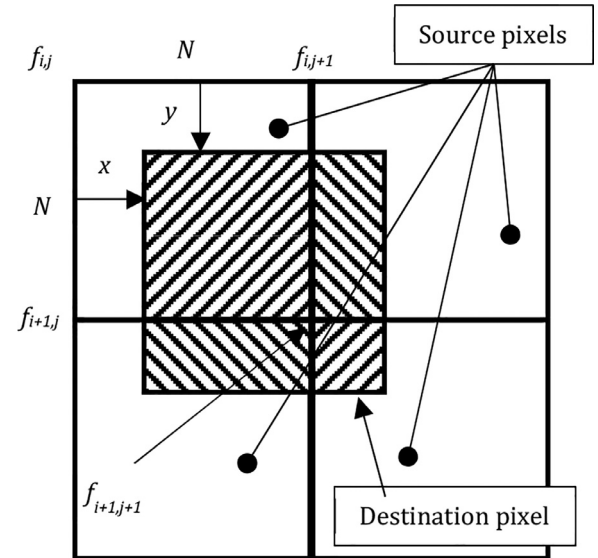
Acknowledgments

Fig. 18. Illustration of area weighting for intensity mapping.

Appendix A

Additional displacement field mapping considerations for hybrid DIC-FE approach

Several different techniques were considered for mapping the displacement data onto the FE discretization. Special attention has to be given to this process due to the inherent noise in the DIC data and the desirable mesh features for proper contour integration in the FE model. Since the DIC data is on a uniformly-spaced grid, this is especially important for the cases that contain cracks that are not oriented at 90° (see Fig. 20).

The first approach assessed for handling data mapping from DIC grid to FE grid was to simply rotate the images prior to performing the image correlation. To rotate the image, the coordinate locations of each pixel in the original image are transformed to new coordinate positions using a simple rotation. Interpolation is then used to map the rotated intensity values onto a uniform grid. For the present work, area weighting approach was utilized. For a given position in the new image, the four surrounding pixels are located as illustrated in Fig. 18.

The resulting intensity value *F* at the destination pixel can then be computed using:

$$F = \frac{1}{N^2}\left[(N-x)(N-y)f_{i,j} + x(N-y)f_{i,j+1} + y(N-x)f_{i+1,j} + xy f_{i+1,j+1}\right]$$

(26)

The key advantage of this method is that the image can be rotated to align it with the local crack coordinates such that the resulting DIC output points would also align to the local crack coordinates. Such an aligned mesh enables formulation of uniformly-sized, symmetric contours for evaluating the domain integral. The key disadvantage, however, is that it requires a rotation of the raw image. This rotation can be problematic because the pixel intensity data in the un-rotated image coordinate system must be interpolated to form the rotated image. Even though several standard image processing techniques are available for performing this interpolation, it produces unwanted degradation to the original image data as shown in the comparison in Fig. 19.

The second approach assessed for handling mapping between the DIC output data and the FE model was to perform the image correlation on the original images, and then perform a mapping operation to rotate the DIC output data relative to an FE mesh that is aligned with the crack. In this approach, the rotated DIC output data points do not align with the
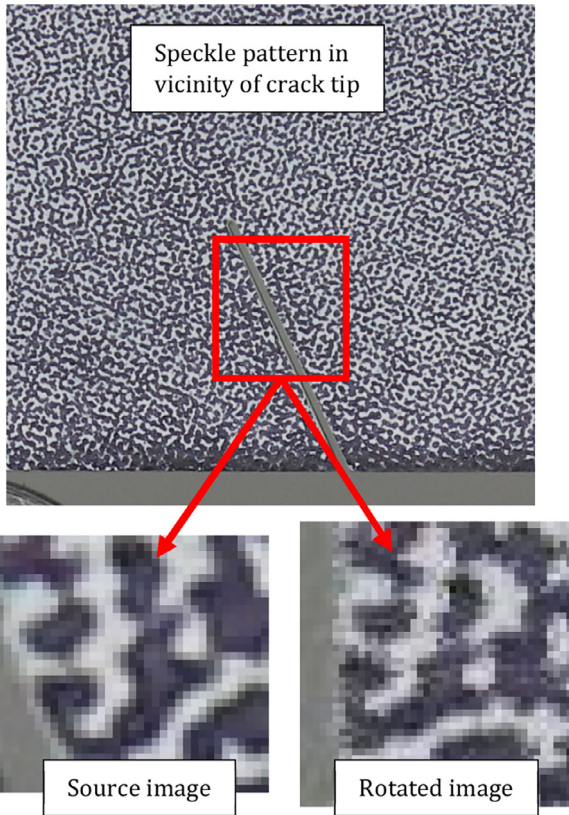
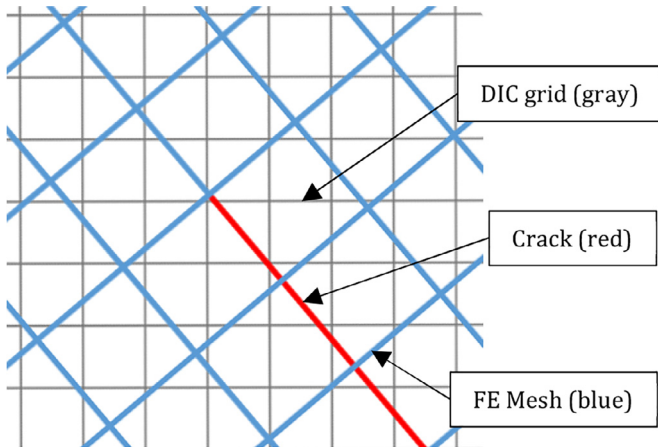**Fig. 19.** Noise introduced into image by pixel rotation process.

Fig. 20. Misaligned DIC and FE grids. (The FE grid is intentionally shown to be coarser than the DIC grid for clarity.).

FE mesh as illustrated in Fig. 20. For the current work, several options were considered including FE meshes that matched the DIC grid as well as coarser or finer mesh sizes for the FE mesh.

Therefore, for a given node in the FE mesh, it is necessary to locate the neighboring DIC output points to determine its displacement. This method is attractive because the use of mapped field quantities in the FE analysis community is commonplace, and therefore, numerous methods can be used for determining the mapped nodal displacements. Many techniques can readily be implemented to perform mapping between significantly dissimilar meshes. For the present work, due to the structured nature of the DIC data, a simple bilinear interpolation method was implemented as,

$$f(x, y) = a_0 + a_1 x + a_2 y + a_3 xy \tag{27}$$

Table 2
Path independence evaluation for 40° case.

Method	K_{II}, Average (MPa/$\sqrt{m}$)	K_{II}, Standard Deviation (MPa/$\sqrt{m}$)	K_{II}, Coefficient Of Variation (%)
No rotations	0.645	0.026	4.0%
Rotate data	0.629	0.050	8.0%
Rotate image	0.624	0.040	6.4%

where the coefficients can be found by solving the following system of linear equations:

$$\begin{bmatrix} 1 & x_1 & y_1 & x_1 y_1 \\ 1 & x_1 & y_2 & x_1 y_2 \\ 1 & x_2 & y_2 & x_2 y_1 \\ 1 & x_2 & y_2 & x_2 y_2 \end{bmatrix} \begin{bmatrix} a_0 \\ a_1 \\ a_2 \\ a_3 \end{bmatrix} = \begin{bmatrix} f(Q_{11}) \\ f(Q_{12}) \\ f(Q_{21}) \\ f(Q_{22}) \end{bmatrix} \tag{27}$$

where $Q_{11} = (x_1, y_1)$, $Q_{12} = (x_1, y_2)$, $Q_{21} = (x_2, y_1)$, and $Q_{22} = (x_2, y_2)$. This method has the advantage that any grid of DIC displacement data can be mapped onto any FE mesh; therefore, the mesh surrounding the crack tip can be structured to whatever is desired depending on the problem of interest. The disadvantage with this method, however, is that again this process introduces undesirable uncertainty and degradation of the data due to numerical interpolation.

The third approach assessed in the present work was to perform DIC on the original images and build an FE mesh that aligns with the DIC output points. Using this method, no information is lost as in the previous two methods. The disadvantage of this method, however, is that the mesh in the vicinity of the crack tip is not well-aligned with the crack. This results in a "stair-stepping" effect along the crack faces and complicates formulation of the node and element sets for contour integral evaluation. For the geometry studied in the present work, this technique was easily implemented for the cases where the crack was at higher angles and therefore the crack tip was not near a boundary. For the lower angle cases, however, the automatic creation of contour sets was less than optimal. Due to the formation of square contour regions, edge effects quickly became apparent in the contour integral output. To address this, a method was developed to manually create circular contours of node and element sets surrounding the crack tip. This allowed evaluation of contours that extended closer to the edge without actually including elements and nodes that were on the actual specimen edge.

To compare these three approaches, the contour independence was assessed in the region of $0.75 \leq {}^r/_B \leq 1.5$ for a given load. This region represents output that should be relatively constant as it is outside the region of crack tip uncertainties, but sufficiently far from the specimen boundary. For this comparison, the average value of stress intensity factor and the standard deviation across the region were computed. The results of this comparison are summarized in Table 2.

As expected the approach involving no rotations and circular contours around the crack tip yields the most consistent value of stress intensity factor in the region of interest (i.e., the standard deviation is the lowest relative to its average value). However, the other two mapping approaches do not introduce an overwhelming amount of noise. Based on these results, neither images nor resulting displacement output data were rotated. However, the other two approaches have potential for applications where their advantages outweigh disadvantages.

Appendix B

Additional SCB specimen considerations

As described in the paper, the SCB specimen geometry offers many features that are beneficial to study mixed mode fracture. Specifically, it is convenient from a fabrication standpoint and it has the ability to achieve a full range of mode mixities, from pure mode-I to pure mode-
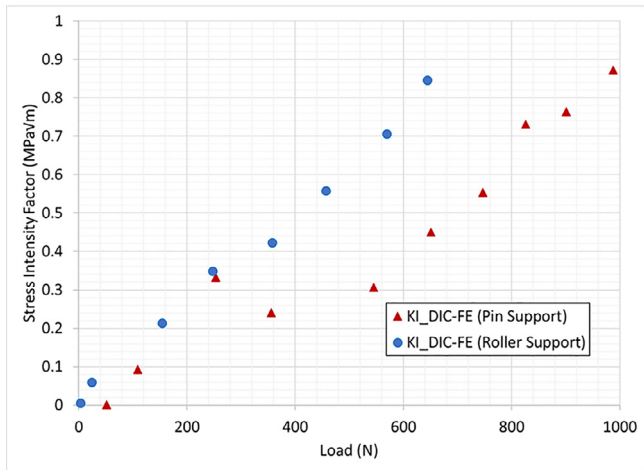
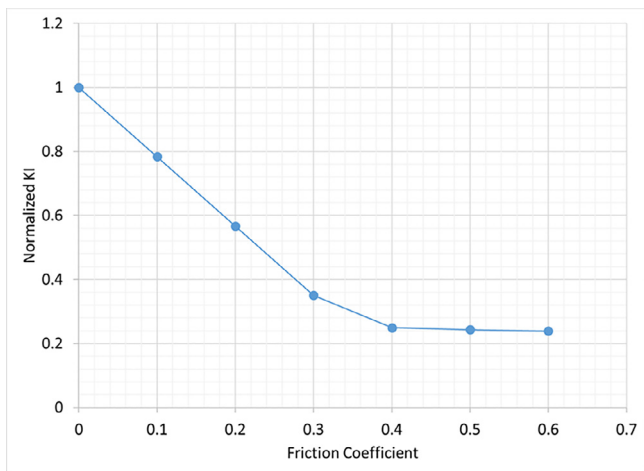**Fig. 21.** Comparison of experimentally measured SIFs obtained from fixed support and roller support fixtures.

Fig. 22. Effect of support pin friction on mode-I stress intensity factor for 90° crack orientation.
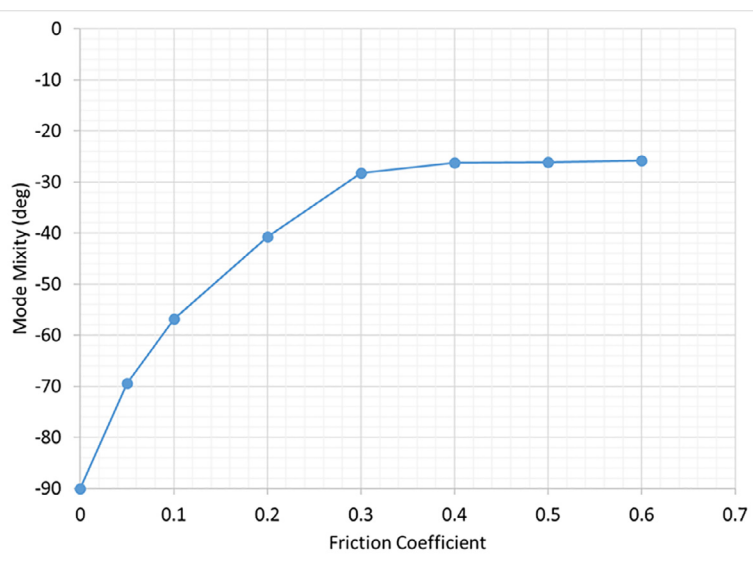

II. However, there are several implementation challenges that must be addressed. First, this specimen geometry has a relatively short support span, S, relative to the radius, R. Furthermore, the ratio of the support span to the crack length, a, is also relatively small. Therefore, there is room for errors due to asymmetry in the support locations relative to the crack. Second, small amounts of lateral load at the supports from friction (in the case of a fixed support pin) and rolling resistance (in the case of a free roller support) have potential negative influence on the results. The typical method for extracting fracture parameters using this geometry usually involves measuring applied force at crack initiation and applying that to a finite element model to infer the critical crack tip parameters such as SIF. While doing so, the lateral components of load at the supports are typically not considered since frictionless contacts are assumed by default.

During the course of conducting experiments using this specimen design, two different support configurations noted above were considered. (Note that the results presented in the paper were generated using a traditional roller support.) Each of the two support points consisted of a steel roller that was free to rotate on a hardened and polished steel pin. Additionally, lubricant was also applied to each pin to further minimize friction. For the mode I case, a separate experiment was conducted that utilized more common fixed support pins that were not free to rotate. The extracted stress intensity factors are plotted versus load for each of the two experiments in Fig. 21.

The slope of the stress intensity factor vs. load history is noticeably different between the two experiments. For instance, the load at which the specimen reached a stress intensity factor of 0.5 MPa$\sqrt{m}$ for the fixed pin support was over 50% higher than the load required to achieve the same value for the roller pin support. Additionally, the SIF values for the pin support seem to suggest a stick-slip behavior between the specimen and the pin. That is, an abrupt drop in SIF value at ~250 N is evident in Fig. 22 followed by an increase with increasing loads. It is suspected that this is largely due to the frictional effects at the support pin creating a closing moment that reduces the crack tip stresses. As the load increases, the frictional force would be proportional to the normal load at the pin.

A finite element model with friction at the two supports was used to test this hypothesis. In the mode I case, the observed/apparent mode I value can be potentially higher than the actual mode I value if friction is not accounted for. The effect of friction on observed mode I behavior is shown in Fig. 22. These results suggest that at a coefficient of friction value of 0.2, which would be representative of an epoxy material siding on a fixed steel pin, the actual mode-I SIF could be roughly 60% of the
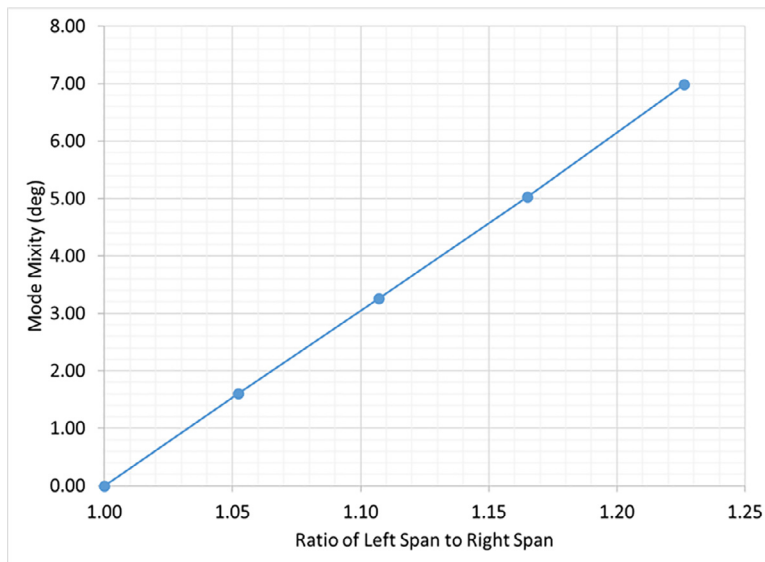
Fig. 23. Effect of support pin friction on mode-mixity for 40° crack orientation which is to be 90° under ideal conditions of zero friction.

Fig. 24. Effect of support asymmetry on mode mixity for 90° crack orientation.

mode-I SIF as observed based on applied load. In mixed mode cases where the vertical load can be significantly higher, this effect could get exacerbated as illustrated in Fig. 23 for the response of mode mixity.

For the mode I case, increase in the friction coefficient can lead to rapid reductions in inferred mode I stress intensity factor. It should also be noted that even in the scenario of a perfectly frictionless rolling support, the rolling resistance between the hardened steel roller and the softer specimen material can have a similar effect, however, it is expected that it would be less severe.

In addition to the effects of lateral frictional forces at the support points, other considerations seem important for this geometry as well. Due to the short support span in the SCB specimen geometry, small amounts of asymmetry in the support location, can introduce relatively significant changes to the mode mixity. In Fig. 24, mode mixity is plotted for various states of misalignment for the 90° crack orientation. A modest asymmetry expressed in terms of the ratio of the left half-span to the right half-span of 1.1 could result in approx. 3° mode-mixity.

Similar observations have been made by other authors [30] where discrepancies between critical stress intensity factors extracted using analytical expressions with failure load approached twice the value of critical stress intensity factors extracted using full-field displacements from DIC. These observations and the ones in the present work underscore the importance of specimen alignment and support configuration when using SCB specimen geometry.

References

[1] Peters W, Ranson W. Digital imaging techniques in experimental stress analysis. Opt Eng 1982;21(3):427–32.

[2] Sutton MA, Wolters WJ, Peters WJ, Peters WH, Ranson WF, McNeill SR. Determination of displacements using an improved digital correlation method. Image Vision Comput 1983;1(3):133–9.

[3] Peters WH, Ranson WF, Sutton MA, Chu T, Anderson J. Applications of digital correlation methods to rigid body mechanics. Opt Eng 1983;22(6):738–42.

[4] Chu TC, Ranson MA, Sutton MA. Applications of digital-image-correlation techniques to experimental mechanics. Exp Mech 1985;25(3):232–44.

[5] Sanford RJ. Application of the least-squares method to photoelastic analysis. Exp Mech 1980;20:192–7.

[6] Sanford RJ. Determining fracture parameters with full-field optical methods. Exp Mech 1989;29:241–7.

[7] McNeill SR, Peters WH, Sutton MA. Estimation of stress intensity factor by digital image correlation. Eng Fract Mech 1987;28:101–12.

[8] Andanto-Buento J, Lambros J. Investigation of crack growth in functionally graded materials using digital image correlation. Eng Fract Mech 2002;69:1695–711.

[9] Yoneyama S, Takashi M. Automatic determination of stress intensity factor utilizing digitial image correlation. J Jpn Soc Exp Mech 2001;1:202–6.

[10] Kirugulige MS, Tippur HV. Measurement of surface deformations and fracture parameters for a mixed-mode crack driven by stress waves using image correlation technique and high-speed photography. Strain 2009;45:108–22.

[11] Kirugulige MS, Tippur HV, Denney TS. Measurement of transient deformations using digital image correlation method and high-speed photography: application to dynamic fracture. Appl Opt 2007;46:5083–96.

[12] Yoneyama S, Arikawa S, Kusayanagi S, Hazumi K. Evaluating J-integral from displacement fields measured by digital image correlation. Strain 2014;50:147–60.

[13] Yates JR, Zanganeh M, Tai YH. Quantifying crack tip displacement fields with DIC. Eng Fract Mech 2010;77:2063–76.

[14] Hareesh TV, Chiang FP. Integrated experimentalfinite element approach to study elastoplastic crack tip field. Eng Fract Mech 1988;31:451–61.

[15] Dubois F, Meite M, Pop O, Absi J. Characterization of timber fracture using the digital image correlation technique and finite element method. Eng Fract Mech 2012;96:107–21.

[16] Isaac JP, Dondeti S, Tippur HV. Crack initiation and growth in additively printed ABS: effect of print architecture studied using DIC. Add Manufactur 2020.

[17] Blaber J, Adair B, Antoniou A. Ncorr: open-source 2D digital image correlation Matlab software. Exp Mech 2015;55(6):1105–22.

[18] He K, Sun J, Tank X. Guided image filtering. IEEE Trans Pattern Anal Mach Intell 2013;35(6):1397–408.

[19] Shih CF, Moran B, Nakamura T. Energy release rate along a three-dimensional crack front in a thermally stressed body. Int J Fract 1986;30:79–102.

[20] Shih CF, Asaro R. Elastic-plastic analysis of cracks on bimaterial interfaces: part I: small scale yielding. J Appl Mech 1988;55(2):299–316.

[21] Chong KP, Kuruppu MD. New specimen for fracture toughness determination for rock and other materials. Int J Fract 1984;26:R49–62.

[22] Chong KP, Kuruppu MD, Kuszmaul JS. Fracture toughness determination of rocks with core-based specimens. SEM/RILEM international conference on fracture of concrete and rocks Texas; 1987.

[23] Lim IL, Johnston IW, Choi SK. Stress intensity factors for semi-circular specimens under three-point bending. Eng Fract Mech 1993;44(3):363–82.

[24] ASTM D638-14 - standard test method for tensile properties of plastics. West Conshohocken, PA: ASTM International; 2014.

[25] Pan B, Lu Z, Xie H. Mean intensity gradient: An effective global parameter for quality assessment of the speckle patterns used in digital image correlation. Opt Lasers Eng 2010;48:469–77.

[26] Westergaard HM. Bearing pressure and cracks. J Appl Mech 1939;6:49–53.

[27] Williams ML. On the stress distribution at the base of a stationary crack. J Appl Mech 1957;24:109–14.

[28] Smith DJ, Ayatollahi MR, Pavier MJ. The role of T-stress in brittle fracture for linear elastic materials under mixed-mode loading. Fatigue Fract Eng Mater Struct 2001;24:137–50.

[29] Simulia, *Abaqus reference manual,* 2020.

[30] Campione I, Brugo TM, Minak G, Tomic JJ, Bogojevic N, Kostic SN. Investigation by digital image correlation of mixed mode I and II fracture behavior of metallic IASCB specimens with additive manufactured crack-like notch. Metals 2020;10(3):400.